

NGDEEP: A New Non-Parametric Measure of Local Star-Formation and Attenuation at Cosmic Noon

GRACE M. FORREY ,¹ RAYMOND C. SIMONS ,² JONATHAN R. TRUMP ,¹ LU SHEN ,^{3,4} ANTON M. KOEKEMOER ,⁵ MICAELA B. BAGLEY ,^{6,7} STEVEN L. FINKELSTEIN ,^{6,8} CASEY PAPOVICH ,^{3,4} AND NOR PIRZKAL ,⁹

¹Department of Physics, 196A Auditorium Road, Unit 3046, University of Connecticut, Storrs, CT 06269, USA

²Department of Engineering and Physics, Providence College, 1 Cunningham Sq, Providence, RI 02918 USA

³Department of Physics and Astronomy, Texas A&M University, College Station, TX, 77843-4242 USA

⁴George P. and Cynthia Woods Mitchell Institute for Fundamental Physics and Astronomy, Texas A&M University, College Station, TX, 77843-4242 USA

⁵Space Telescope Science Institute, 3700 San Martin Drive, Baltimore, MD 21218, USA

⁶Department of Astronomy, The University of Texas at Austin, Austin, TX, USA

⁷Astrophysics Science Division, NASA Goddard Space Flight Center, 8800 Greenbelt Rd, Greenbelt, MD 20771, USA

⁸Cosmic Frontier Center, The University of Texas at Austin, Austin, TX, USA

⁹ESA/AURA Space Telescope Science Institute

ABSTRACT

We introduce a new non-parametric technique to quantify the spatially-resolved relationship between the local star-formation rate (SFR) and dust attenuation. We then apply it to 14 star-forming galaxies at $1.0 < z < 2.5$ using JWST/NIRISS slitless spectroscopy from the NGDEEP survey. First, we construct spatially resolved (~ 1 kpc per pixel) Balmer decrement ($H\alpha/H\beta$) maps of these galaxies and derive their corresponding dust attenuation and intrinsic SFR maps. We then rank-order the map pixels by attenuation and construct a cumulative distribution curve of the total SFR as a function of increasing attenuation. We define $A_{10\%}^{\text{SFR}}$, $A_{50\%}^{\text{SFR}}$, and $A_{90\%}^{\text{SFR}}$ as the dust attenuation levels behind which 10%, 50%, and 90% of the total integrated SFR is screened, respectively. These metrics quantify the probability that a given star-forming region lies behind a given level of attenuation. Across the full sample, 50% of the local star formation occurs behind an attenuation of 3.41 mag or higher ($A_{50\%}^{\text{SFR}}$). This indicates that the bulk of star formation in these galaxies is significantly attenuated by dust. The value of $A_{10\%}^{\text{SFR}}$ equals 1.45 for the average profile, indicating that even the least attenuated star-forming regions are still highly attenuated. The globally measured attenuation more closely matches $A_{10\%}^{\text{SFR}}$ than $A_{50\%}^{\text{SFR}}$. This suggests that the global value is weighted toward the least dust-obscured star-forming regions and significantly underestimates the typical attenuation a star-forming region encounters. Our results demonstrate a new approach for understanding the extremely dusty local conditions of the star-forming interstellar medium in SF galaxies at cosmic noon.

1. INTRODUCTION

Dust is a key component of mass in galaxies. Dust traces cold star-forming gas, and so is closely tied with the local star-formation and stellar mass growth of galaxies. Dust also helps regulate the chemical composition of the interstellar medium (ISM). It acts as a catalyst for the creation of molecular hydrogen and as a shield from harsh UV radiation, enabling conditions for the collapse of giant molecular clouds (H.-J. Park et al. 2024). Dust is also a nuisance, attenuating both stel-

lar and nebular emission and posing a major challenge for interpreting observations of galaxies. Understanding the local relationship between dust and star formation is therefore essential for determining how dust both regulates and obscures star-forming activity within galaxies.

The Balmer decrement, defined as the ratio of the hydrogen recombination lines $H\alpha/H\beta$, provides a direct probe of dust attenuation in star-forming regions. The intrinsic ratio is well understood from atomic physics under typical nebular conditions (D. E. Osterbrock & G. J. Ferland 2006). In such conditions, deviations from this intrinsic value indicate differential attenuation that preferentially suppresses $H\beta$ emission. Consequently, the

observed Balmer decrement is routinely used to measure color excess and to infer appropriate dust-corrections in both integrated and spatially-resolved studies (see e.g., [S. Salim & D. Narayanan 2020](#) and references therein). Until recently, however, spatially-resolved Balmer decrement maps were only available for nearby galaxies, due to the limited sensitivity and resolution of infrared instrumentation at high redshift. Recent advances in infrared space-based instrumentation, especially with the launch of *JWST* ([J. P. Gardner et al. 2023](#)), have opened up new avenues for spatially-resolved studies of dust attenuation and star-formation in high-redshift galaxies ([J. Matharu et al. 2023, 2024, 2025](#); [L. Shen et al. 2024](#)). The epoch around redshift $z \approx 2$, commonly referred to as “cosmic noon,” marks a peak in the cosmic star formation rate and is an intense period of mass growth and structural evolution for galaxies ([P. Madau & M. Dickinson 2014](#)). Measurements of the spatially-resolved characteristics of dust and SFR in galaxies at this epoch provide important insight into how galaxies build and grow during this critical period ([N. M. Förster Schreiber & S. Wuyts 2020](#)).

The slitless grism spectrographs of the Wide Field Camera 3 on the *Hubble Space Telescope* (HST) enabled the first statistical probes of the spatial distribution of $\text{H}\alpha$ and $\text{H}\beta$ with high-resolution at these redshifts ([E. J. Nelson et al. 2016](#); [J. Matharu et al. 2023](#)). More recently, the NIRISS and NIRCam grisms on the *JWST* observatory have provided a major step forward in this domain, offering slitless spectroscopy with unprecedented sensitivity and spatial resolution ([J. Matharu et al. 2023, 2024](#); [L. Shen et al. 2024](#); [J. Matharu et al. 2025](#)).

In this work, we use *JWST*/NIRISS slitless spectroscopy and imaging from The Next Generation Deep Extragalactic Exploratory Public (NGDEEP) Survey ([M. B. Bagley et al. 2023](#); [N. Pirzkal et al. 2024](#)) to map the Balmer decrement across 14 star-forming galaxies at $1.0 < z < 2.5$. The NGDEEP dataset allows us to study the local relationship between the dust attenuation and the star-formation rate in these systems and to diagnose the reliability of globally-derived measurements of dust attenuation. The sample is selected from the parent sample of [L. Shen et al. \(2024\)](#) and includes galaxies with high signal-to-noise (SNR) integrated detections of both $\text{H}\alpha$ and $\text{H}\beta$.

We also introduce a new non-parametric analysis that quantifies the cumulative SFR as a function of the local dust attenuation acting on its light. Conceptually, this approach asks: how much star formation lies behind how much dust? We argue that this approach provides a

valuable new view on the link between star formation and dust attenuation on the local level.

Throughout this paper, all magnitudes are presented in the AB system ([J. B. Oke & J. E. Gunn 1983](#); [M. Fukugita et al. 1996](#)). Where relevant, we adopt a flat ΛCDM Plank 2018 ([N. Aghanim et al. 2020](#)) cosmology with $H_0 = 67.66 \text{ km s}^{-1} \text{ Mpc}^{-1}$, $\Omega_{\text{m},0} = 0.30966$, and $\Omega_{\text{b},0} = 0.04897$). This cosmology also assumes $T_{\text{CMB}} = 2.7255 \text{ K}$, $N_{\text{eff}} = 3.046$, and a minimal neutrino mass sum of 0.06 eV.

2. DATA AND SAMPLE SELECTION

2.1. Data and Processing

The galaxies studied in this paper lie in the Hubble Ultra Deep Field (HUDF; originally presented by [S. V. W. Beckwith et al. 2006](#)). They were observed with the *JWST* NIRISS Wide Field Slitless Spectrograph (WFSS) as a part of the Next Generation Deep Extragalactic Exploratory Public Survey (NGDEEP; [M. B. Bagley et al. 2023](#)). The WFSS dataset from NGDEEP is described in detail in [M. B. Bagley et al. \(2023\)](#), [N. Pirzkal et al. \(2024\)](#), [L. Shen et al. \(2024\)](#), and [L. Shen et al. \(2025\)](#).

The NGDEEP observations utilize the GR150R and GR150C grisms with the F150W, F115W, and F200W filters. The exposure time in F150W is 82458 s, in F115W is 185531 s, and in F200W is 61844 s. The F150W and F200W observations include 12 individual exposures and the F115W observations include 36 individual exposures. Combined, these filters cover a wavelength range of $1 - 2.2\mu\text{m}$. The NGDEEP NIRISS spectroscopy reaches a 1D line flux of $\approx 1.35 \times 10^{-18} \text{ erg s}^{-1} \text{ cm}^{-2}$ ([L. Shen et al. 2025](#)).

The NIRISS grism observations were taken in two position angles (PA) in each of GR150C and GR150R grisms, providing a total of four independent dispersion PAs. This approach reduces the degeneracy between wavelength and sky position that occurs when spectra overlap along a single dispersion axis ([N. Pirzkal et al. 2018](#)). The use of two orientations enables the majority of overlapping sources to be effectively deblended, allowing for a more reliable extraction of the resolved emission line structure ([P. J. Watson et al. 2025](#)).

2.2. Grism Data Reduction and Extractions

The NGDEEP imaging and slitless spectroscopy was processed in [L. Shen et al. \(2024\)](#) and [L. Shen et al. \(2025\)](#) using the Grism redshift and line analysis software `Grizli` ([G. Brammer 2022](#)). `Grizli` provides a full end-to-end processing of NIRISS imaging and spectral products, including astrometric correc-

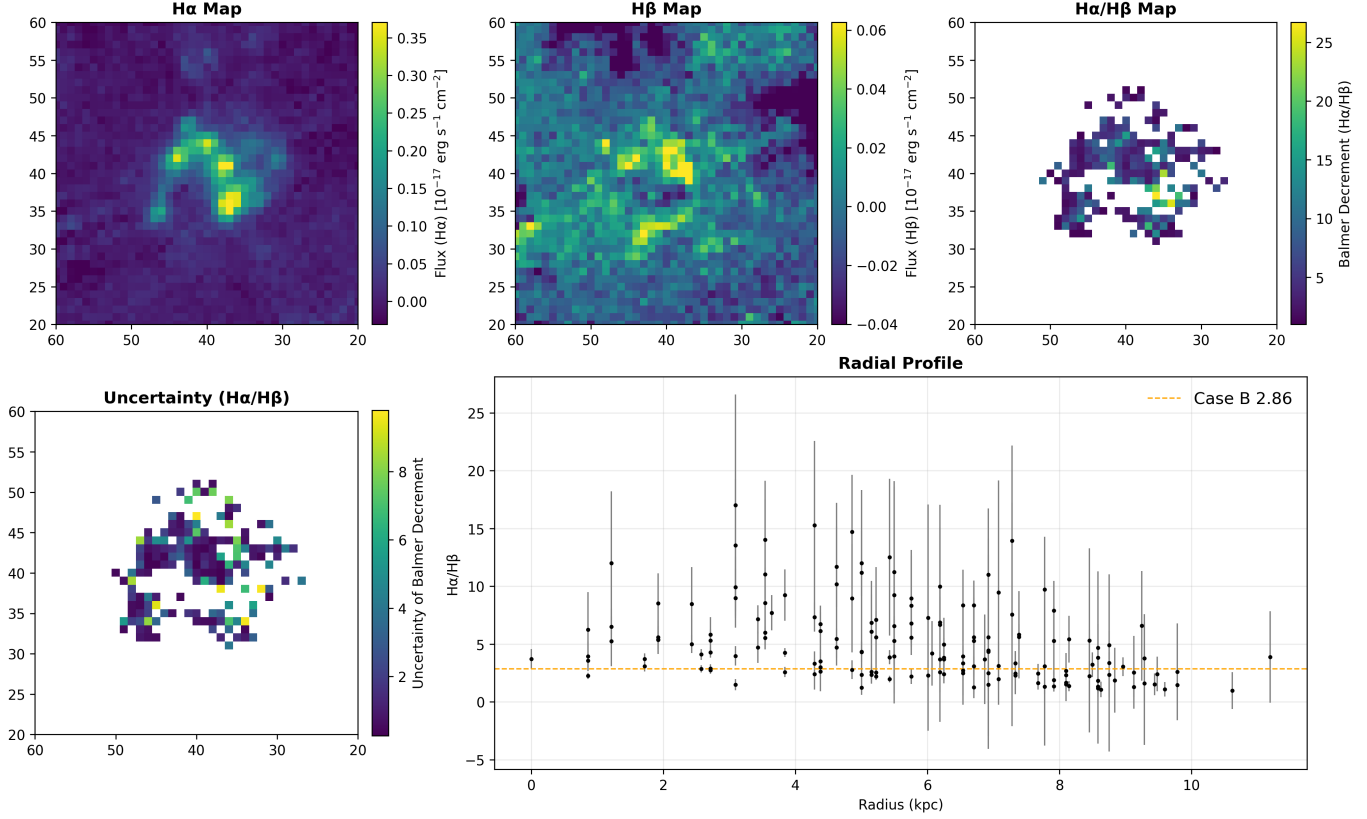


Figure 1. The maps derived for an example galaxy, `ngdeep_00503`, are shown. The top row includes the $\text{H}\alpha$ flux map (left), $\text{H}\beta$ flux map (middle), and the segmented Balmer decrement ($\text{H}\alpha/\text{H}\beta$) map (right). The bottom row shows the uncertainty of the Balmer decrement map (left) and the Balmer decrement radial profile (right). Each point of the radial profile corresponds to an individual pixel. The orange dashed line marks the intrinsic Balmer decrement expected for case-B recombination.

tions, alignment, modeling, extracting, and fitting full continuum+emission-line models. `Grizli` constructs emission line maps using the drizzling technique to combine multiple image exposures or data frames of the contamination and continuum subtracted 2D spectral beams back to the imaging plane. The JWST/NIRISS imaging is used to scale the data to match the total fluxes in the direct images. The emission-line maps are derived using a pixel scale of $0\farcs1$. The resolved SED fitting and $\text{H}\alpha$ emission maps enable quantitative analysis of spatially-resolved galaxy properties with a resolution of ~ 1 (proper) kpc (L. Shen et al. 2024). The uncertainties are calculated using the drizzle weights from the constituent beam pixels. For further details on `Grizli` and its data products, we refer the reader to V. Estrada-Carpenter et al. (2019), C. Papovich et al. (2022), X. Wang et al. (2022), J. Matharu et al. (2021), R. C. Simons et al. (2021, 2023), G. Noirot et al. (2023), and J. Matharu et al. (2023).

2.3. Sample Selection

The sample studied in this paper is selected from the parent sample of L. Shen et al. (2024). Galaxies in

the L. Shen et al. (2024) parent sample are required to have $\text{SNR} > 20$ for the total $\text{H}\alpha$ line flux (integrated over all pixels), and to have at least 50 individual pixels with $\text{H}\alpha$ flux measured with $\text{SNR} > 3$. We use visual inspection to exclude galaxies showing contamination in one or more of their emission line maps from imperfect continuum subtraction. The `Grizli`-derived redshifts are consistent with previous ground-based and space-based spectroscopic measurements of our sources, where L. Shen et al. (2024) found a median offset of only $\Delta z/(1+z) = 0.002$.

We down-select the L. Shen et al. (2024) sample for those galaxies with both $\text{H}\alpha$ and $\text{H}\beta$ emission line coverage in order to measure the Balmer decrement. This selection imposes a redshift window of $1.0 < z < 2.4$. The final sample contains 14 galaxies.

3. MEASUREMENTS

3.1. Balmer Decrement

For each galaxy, we use the $\text{H}\alpha$ and $\text{H}\beta$ maps produced by `Grizli` to derive a map of the Balmer decrement ($\text{H}\alpha/\text{H}\beta$) and its uncertainty. The Balmer decrement map and emission line maps for one of the galaxies in

our sample are shown in Figure 1. The radial profile of $H\alpha/H\beta$ for this same source is also shown in this Figure.

We select contiguous pixels belonging to the galaxy by constructing a segmentation map (using `photutils.segmentation`) on the Balmer decrement map. This process selects spatially connected regions with both lines detected and excludes isolated noise fluctuations.

The Balmer emission lines are produced from the recombination and subsequent “electron avalanche” to the $n = 2$ level of hydrogen atoms in the interstellar medium (ISM). We assume case-B recombination, which is appropriate for galaxies where the interstellar medium is optically thick to Lyman series photons. Under case-B recombination, the intrinsic Balmer decrement weakly depends on temperature and density. Adopting $n_e = 100 \text{ cm}^{-3}$ and $T_e = 10^4 \text{ K}$, we use $\frac{H\alpha}{H\beta} \approx 2.86$ (D. E. Osterbrock & G. J. Ferland 2006; W. McClymont et al. 2024; D. H. Menzel & J. G. Baker 1937; J. G. Baker & D. H. Menzel 1938). For a given total dust attenuation, the bluer $H\beta$ line will be more attenuated than the redder $H\alpha$ line. The observed $H\alpha/H\beta$ ratio thus provides a measure of the dust attenuation.

Qualitative inspection of the Balmer-decrement maps shows that the regions where the ratio is high appear in coherent pixel groups rather than being isolated. The highest Balmer decrement values are centrally concentrated in 13 of the 14 galaxies. This trend is quantitatively supported by the radial profiles, which show a systematic decrease in decrement with increasing distance from each galaxy’s center (see example in Figure 1). The remaining galaxy exhibits a weak inversion of this pattern, with slightly higher decrement values in the outskirts than in the central regions. This behavior is likely driven by gaps in the Balmer decrement map for this galaxy: due to the reliability thresholds applied when measuring decrement values, these gaps are preferentially located near the center, which may bias the observed radial trend.

As described in the next subsection, we adopt a D. Calzetti (1997) dust law to derive maps of the attenuation at $H\alpha$ ($A(H\alpha)$), and to dust correct the $H\alpha$ flux maps. The resulting maps of dust attenuation indicate attenuation that generally increases toward the centers of the galaxies. This is consistent with previous spatially-resolved studies of star-forming galaxies across a range of redshifts (S. Tacchella et al. 2018; S. Wuyts et al. 2012; W. Wang et al. 2017; S. Hemmati et al. 2015).

3.2. Attenuation at $H\alpha$

Following I. G. Momcheva et al. (2013), we derive the attenuation at $H\alpha$ by first calculating the Balmer color excess,

$$E(B - V) = \frac{E(H\beta - H\alpha)}{\kappa(H\beta) - \kappa(H\alpha)} \quad (1)$$

$$= \frac{-2.5}{\kappa(H\beta) - \kappa(H\alpha)} \times \log_{10} \left[\frac{(H\alpha/H\beta)_{\text{intrinsic}}}{(H\alpha/H\beta)_{\text{obs}}} \right]$$

where we assume the case-B recombination value of $(H\alpha/H\beta)_{\text{intrinsic}} = 2.86$ (D. E. Osterbrock & G. J. Ferland 2006). We adopt the D. Calzetti (1997) attenuation law to compute $\kappa(\lambda)$ for both $H\alpha$ and $H\beta$. For $\kappa(H\beta)$ and $\kappa(H\alpha)$,

$$\kappa(H\beta) = 2.656(-2.156 + 1.509/\lambda(H\beta) - 0.198/(\lambda(H\beta))^2 + 0.011/(\lambda(H\beta))^3) + 4.88$$

$$\kappa(H\alpha) = [(1.86 - 0.48/\lambda(H\alpha))/\lambda(H\alpha) - 0.1]/\lambda(H\alpha) + 1.73 \quad (2)$$

where $\lambda(H\beta) = 0.4863 \mu\text{m}$ and $\lambda(H\alpha) = 0.6565 \mu\text{m}$. The attenuation at $H\alpha$ is then,

$$A(\lambda) = \kappa(H\alpha)E(B - V) \quad (3)$$

To test the sensitivity of our results to the choice of attenuation law, we repeat the above calculations using the N. A. Reddy et al. (2020) attenuation law:

$$\kappa(\lambda) = -0.816 + \frac{2.286}{\lambda} \quad (4)$$

Using this law, we recalculate $E(B - V)$, $A(H\alpha)$, and the corresponding dust-corrected SFR following the procedure described above.

To ensure reliable attenuation estimates, we create a mask for pixels whose uncertainty in $A(H\alpha)$ exceeds 10. This selection removes pixels with low-SNR in the $H\alpha$ or $H\beta$ map. The resulting mask is then applied to all subsequent maps used in the analysis, including those of the dust-corrected $H\alpha$ luminosity and SFR.

3.3. Dust-Corrected Star Formation

We derive the dust-corrected star formation rate of each pixel using the R. C. Kennicutt & N. J. Evans (2012) relation:

$$\log_{10} SFR(M_{\odot} \text{yr}^{-1}) = \log_{10} L_{H\alpha} - 41.27 \quad (5)$$

We calculate the attenuation corrected $H\alpha$ luminosity:

$$L_{H\alpha} = f_{\text{intrinsic}} \times 4\pi d_L^2 \quad (6)$$

where $f_{\text{intrinsic}}(H\alpha) = f_{\text{obs}}/10^{-0.4 \times A(H\alpha)}$, $f_{\text{obs}}(H\alpha)$ is the observed flux at $H\alpha$ in each pixel, and d_L is the luminosity distance of the galaxy determined by the redshift

ID					SED Based		H α Based	
	R.A.	Decl.	Redshift		Stellar Mass	SFR	Corrected SFR	Uncorrected SFR
	deg	deg			$\log(M_\odot)$	$\log(M_\odot/yr)$	$\log(M_\odot/yr)$	$\log(M_\odot/yr)$
ngdeep_00503	53.16690	-27.79882	1.992		10.7 ± 0.17	2.52 ± 0.10	2.09 ± 0.056	1.19 ± 0.002
ngdeep_01585	53.14928	-27.78859	1.897		10.11 ± 0.12	1.74 ± 0.17	2.05 ± 0.048	1.06 ± 0.0018
ngdeep_01729	53.16167	-27.78750	1.848		10.58 ± 0.07	1.77 ± 0.15	1.47 ± 0.116	0.53 ± 0.0049
ngdeep_02347	53.17432	-27.78260	1.997		10.41 ± 0.08	1.62 ± 0.16	1.44 ± 0.085	0.75 ± 0.0039
ngdeep_02703	53.15568	-27.77936	1.844		10.56 ± 0.07	1.77 ± 0.15	1.59 ± 0.046	1.04 ± 0.0018
ngdeep_02748	53.14922	-27.77888	1.842		10.17 ± 0.07	1.10 ± 0.16	1.69 ± 0.13	0.598 ± 0.0047
ngdeep_03359	53.17606	-27.77377	1.291		10.26 ± 0.1	1.31 ± 0.18	1.69 ± 0.13	0.462 ± 0.0031
ngdeep_03606	53.14618	-27.77110	1.315		10.06 ± 0.1	1.01 ± 0.19	0.843 ± 0.345	0.341 ± 0.0104
ngdeep_03827	53.16635	-27.76864	1.297		10.33 ± 0.09	1.42 ± 0.17	1.69 ± 0.106	0.381 ± 0.0034
ngdeep_01524	53.14511	-27.78949	1.302		9.83 ± 0.12	1.04 ± 0.17	1.39 ± 0.124	0.207 ± 0.0038
ngdeep_02240	53.17825	-27.78315	1.116		9.62 ± 0.09	0.82 ± 0.14	1.17 ± 0.175	0.0528 ± 0.0037
ngdeep_03326	53.14420	-27.77362	1.899		9.33 ± 0.1	0.94 ± 0.18	1.44 ± 0.094	0.622 ± 0.0032
ngdeep_03627	53.15447	-27.77151	2.221		9.84 ± 0.11	1.01 ± 0.08	1.81 ± 0.0511	1.18 ± 0.0025
ngdeep_03844	53.15231	-27.77014	1.839		9.76 ± 0.09	1.13 ± 0.14	1.57 ± 0.141	0.778 ± 0.0038

Table 1. Columns 1-4 report the ID, right ascension, declination, and redshift of the galaxies in our sample. Columns 5 and 6 report the integrated SED fits (stellar mass and SFR) from L. Shen et al. (2024). Columns 7 and 8 report the H α -based SFR measurements (corrected and uncorrected for dust, respectively).

of the galaxy. The dust-corrected star formation rate is calculated for each pixel in the unmasked H α map. We then compute a total star-formation rate by integrating over the segmentation map of the source. This SFR is reported in Table 1.

When comparing the D. Calzetti (1997) and N. A. Reddy et al. (2020) attenuation laws, we produce SFR maps and radial profiles that are similar in structure but with differences in normalization. In other words, the overall shapes of the radial profiles are similar between the two methods even as the amplitude of the SFR and attenuation increases when using the N. A. Reddy et al. (2020) law instead of D. Calzetti (1997).

3.4. SED Fitting

We compare the total star formation rates estimated from two independent approaches: (i) the sum of the SFR of the individual pixels (described above) and (ii) fits to the global spectral energy distribution (SED) as measured in L. Shen et al. (2024).

The SED fitting was carried out with the **Code Investigating GALaxy Emission** (CIGALE) code, which estimates stellar masses and star formation rates through joint modeling of stellar, nebular, and dust emission constrained by the available multi-wavelength photometry (M. Boquien et al. 2019; G. Yang et al. 2019). The dust emission is modeled using templates from D. A. Dale et al. (2014). These templates model the star-forming component as $dM_d(U) \propto U^{-\alpha} dU$, where M_d is the mass of the dust, and U is the radia-

tion field intensity. L. Shen et al. (2024) allow α to vary from 0.25-4 in their analysis. We refer the reader to Section 3.1 in L. Shen et al. (2024) for more details.

We adopt the $\log(M_*/M_\odot)$ and $\log(SFR/M_\odot yr^{-1})$ values reported in Table 2 of L. Shen et al. (2024) and include them in Table 1 of this paper for the galaxies in our sample. We note that the SED-derived SFRs are averaged over ~ 100 Myr, while the H α -based SFRs trace only the most recent ~ 10 Myr of star formation. Recent variations in star formation, such as a recent starburst or quenching episode, can therefore produce offsets in the comparison even when both methods are internally consistent.

In Figure 2, we examine the relationship between $\log(SFR_{\text{Balmer}})$ and $\log(SFR_{\text{SED}})$ across the sample. Because pixels with large $A(\text{H}\alpha)$ uncertainties are excluded, faint, low-signal-to-noise H β pixels are preferentially removed. This selection effect will lead to a modest underestimation of the dust-corrected H α SFR relative to the SED-derived values.

As shown in Figure 2, several galaxies deviate significantly from the one-to-one relation. We quantify this offset as

$$\Delta \log(\text{SFR}) = \log(\text{SFR}_{\text{Balmer}}) - \log(\text{SFR}_{\text{SED}}) \quad (7)$$

and identify five galaxies with $|\Delta \log(\text{SFR})| > 0.4$, indicating potentially significant discrepancies between the two SFR estimators.

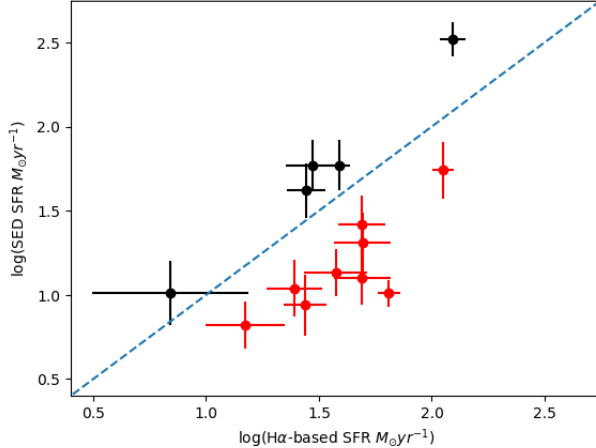


Figure 2. The H α -based SFR versus the SED-derived SFR for the galaxy sample is shown. Galaxies are color-coded black and red if they fall above or below the blue one-to-one line, respectively.

Four galaxies exhibit systematically higher SFR_{Balmer} values than their SED-inferred rates: `ngdeep_02748`, `ngdeep_03627`, `ngdeep_03326`, and `ngdeep_03844`. The galaxy `ngdeep_03627` stands out as an extreme case ($\Delta \log(\text{SFR}) \sim +0.8$). This may reflect unusually strong central dust attenuation or limitations in the assumed SED modeling parameters for this source. In contrast, galaxy `ngdeep_00503` exhibits a negative offset ($\Delta \log(\text{SFR}) \sim -0.45$), suggesting that the Balmer-based estimate may underestimate the total star formation rate, potentially due to under-corrected dust extinction or incomplete flux recovery.

Further insight is provided by a qualitative inspection of the Balmer decrement maps and mosaic images. Galaxy `ngdeep_02748` shows evidence of H α contamination, necessitating a custom restrictive mask that may bias its measured flux low. Galaxy `ngdeep_03844` is among the faintest of the sample, which could impact the reliability of its SED-based SFR. Meanwhile, `ngdeep_03627`, `ngdeep_03326`, and `ngdeep_00503` exhibit notably clumpy morphologies, which may introduce spatial mismatches or inconsistent attenuation corrections when comparing integrated SFRs.

Overall, these results emphasize the importance of accounting for spatial structure and data quality when interpreting differences between SFR indicators. The identified outliers provide useful case studies for understanding the regimes in which the assumptions underlying either method may begin to break down.

3.5. Star Formation Mass Sequence

In Figure 3, we compare the dust-corrected H α -based SFR of each galaxy to the star-formation mass sequence

at their respective redshifts. The latter is taken from the polynomial relations presented in K. E. Whitaker et al. (2014). The galaxies in our sample lie on or slightly above the mass sequence at their respective redshifts. The median enhancement increases modestly towards higher redshifts, from $\sim 2.5 \times$ at $1.0 < z < 1.5$, $\sim 3.3 \times$ at $1.5 < z < 2.0$, and $\sim 3.2 \times$ at $2.0 < z < 2.5$. Of the sample, 10 of the 14 galaxies lie above the mass sequence.

The galaxies lying above the star-forming mass sequence exhibit a median enhancement of approximately a factor of 2.6 in star formation relative to their expected rate at their stellar mass and redshift. Systems offset by more than 0.3 dex show typical enhancements of $\sim 3 \times$, while only a small subset exceed 0.6 dex above the relation, corresponding to starburst-level activity with star formation rates roughly seven times higher than the mass-sequence expectation.

In short, the galaxies in our sample are generally more highly star-forming than the overall population at their redshifts.

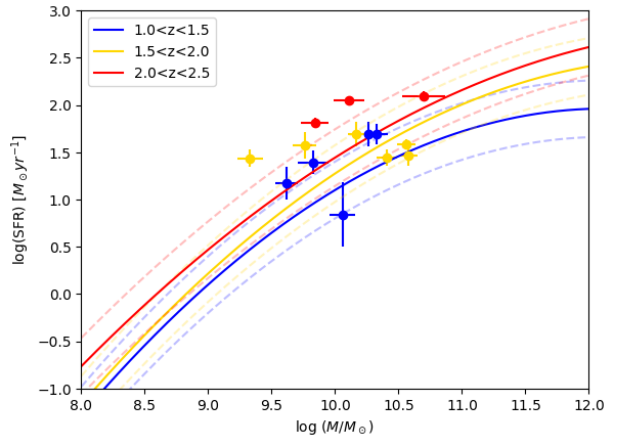


Figure 3. The dust corrected H α -based SFR versus SED-calculated stellar mass is shown for the galaxies in our sample. The solid lines denote the star formation mass sequence lines at the redshifts of the galaxies in our sample (K. E. Whitaker et al. 2014). The red galaxies and lines represent $2.0 < z < 2.5$. The yellow galaxies and lines represent $1.5 < z < 2.0$. The blue galaxies and lines represent $1.0 < z < 1.5$. The dashed lighter lines bound ± 0.3 dex from their respective relation.

4. THE CUMULATIVE STAR-FORMATION RATE AS A FUNCTION OF DUST ATTENUATION

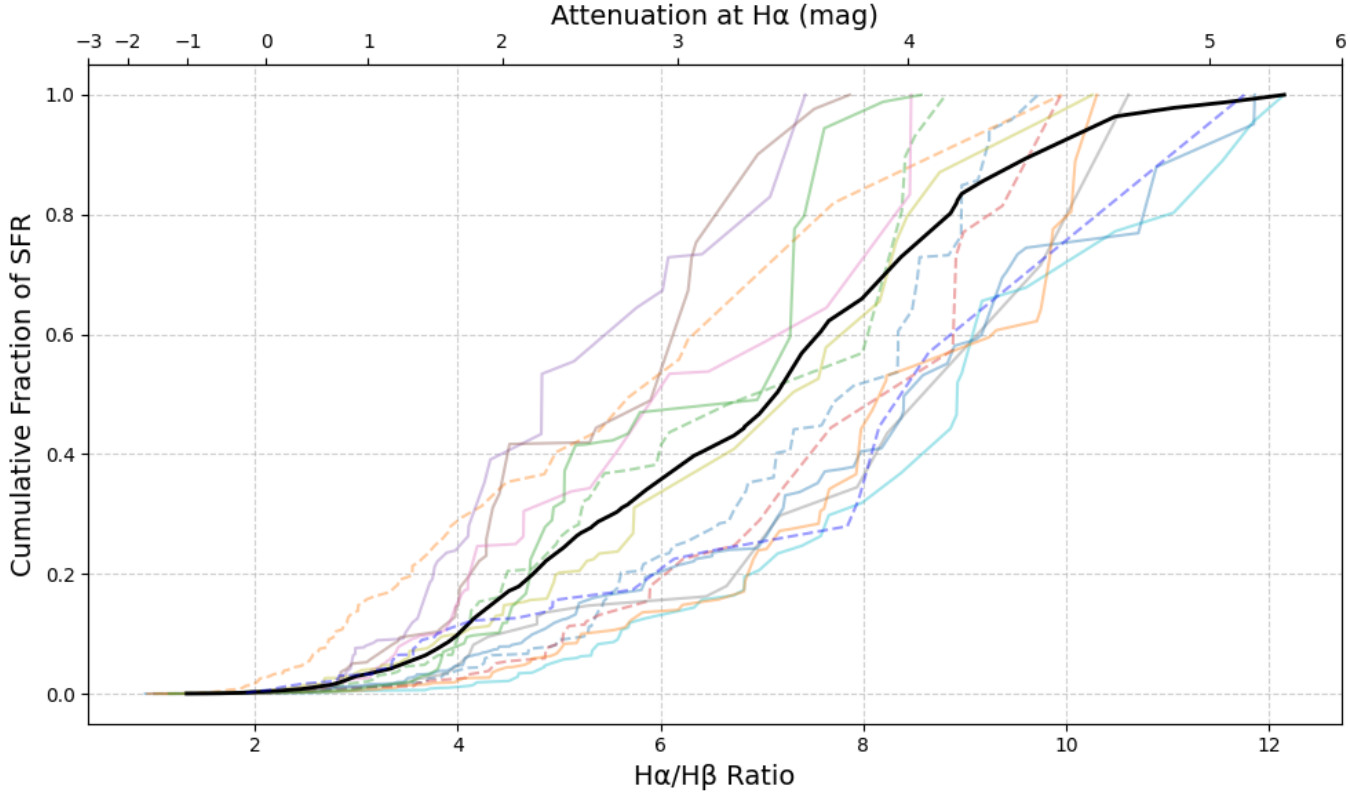


Figure 4. The cumulative distribution of the dust corrected star formation rate as a function of the observed $\text{H}\alpha/\text{H}\beta$ emission line ratio is shown. The top axis indicates the corresponding attenuation at $\text{H}\alpha$ (in magnitudes). Conceptually, this approach quantifies the fraction of star formation at or below a given level of attenuation. The distributions for individual galaxies are shown as dashed and solid colored lines. The average distribution is shown with the bold black line. The nine galaxies below the one-to-one line in Figure 2 are shown by solid lines while the other are shown as dashed lines.

The primary goal of this paper is to assess the spatially-resolved (at the pixel-level) relationship between star-formation and dust attenuation. Specifically, we are interested in quantifying *the fraction* of the star formation that occurs behind *increasing levels* of local dust attenuation in our sample of galaxies.

To probe that question, we introduce a new non-parametric measure: the cumulative distribution of the SFR as a function of the local Balmer decrement ($\text{H}\alpha/\text{H}\beta$). For each galaxy we reduce the 2D maps into 1D arrays sorted by the Balmer decrement of each pixel. We then cumulatively sum the star-formation rate of the map starting from the pixel with the lowest Balmer decrement and ending at the pixel with the highest Balmer decrement. The resulting cumulative curve therefore shows the fraction of a galaxy’s total star formation that is attenuated by dust at or below a given attenuation level.

In Figure 4, we show the cumulative curves for the individual galaxies in the sample (colorful lines) as well as the sample average (black line). The x-axis is expressed in terms of the observed Balmer decrement (bottom axis) and the corresponding attenuation at $\text{H}\alpha$ ($A(\text{H}\alpha)$);

top axis) using the D. Calzetti (1997) dust law. The conclusions in this section are qualitatively similar if we assume the N. A. Reddy et al. (2020) law.

The average curve is constructed from the full collection of SFR and Balmer decrement maps of our sample. This curve smoothly varies with increasing attenuation. The 50th percentile of the cumulative SFR corresponds to a Balmer decrement of $\text{H}\alpha/\text{H}\beta \sim 7$, or an attenuation at $\text{H}\alpha$ of $A(\text{H}\alpha) \sim 3.2$ under the D. Calzetti (1997) law. In other words, this indicates that half of the star-formation rests behind an $A(\text{H}\alpha)$ greater than 3.2. This highlights the prevalence of highly-obscured star formation in these galaxies. The tail of the distribution indicates the presence of star formation in highly obscured clumps reaching $\text{H}\alpha/\text{H}\beta > 10$ ($A(\text{H}\alpha) > 4.6$).

We model (and thus parameterize) the cumulative curves using the functional form:

$$f(x) = A \times 0.5 \times \left[1 + \text{erf} \left(\frac{x - \mu}{\sigma\sqrt{2}} \right) \right] \quad (8)$$

Galaxy ID	$A_{10\%}^{\text{SFR}}$	$A_{50\%}^{\text{SFR}}$	$A_{90\%}^{\text{SFR}}$	Global $A(\text{H}\alpha)$	A	μ	σ
ngdeep_03627	0.7239	1.9418	3.4353	0.9134 ± 0.0580	0.8668	4.7280	1.1882
ngdeep_01585	1.5105	3.3098	3.6021	1.4711 ± 0.0774	0.9923	6.0254	1.6283
ngdeep_00503	2.2761	3.7212	4.3329	2.5491 ± 0.0774	1.9071	9.5227	2.7977
ngdeep_03844	0.9186	2.6973	3.2960	1.2362 ± 0.1082	1.1077	5.6817	1.6490
ngdeep_03326	1.0671	2.7162	4.0226	1.2219 ± 0.1097	0.9507	5.9956	1.9206
ngdeep_02240	1.6071	4.0750	4.7527	1.3327 ± 0.1502	7.4902	16.2298	5.0232
ngdeep_01524	1.2717	3.4685	4.2907	0.4144 ± 0.0909	1.1735	7.5491	2.4722
ngdeep_03827	2.4929	4.2204	5.1886	2.4695 ± 0.1677	1.1073	9.1953	2.5083
ngdeep_03359	1.8809	4.0024	5.0501	1.4128 ± 0.1067	1.1484	8.9046	2.8661
ngdeep_02748	2.2379	3.8876	4.6791	2.1515 ± 0.1986	1.4925	9.7330	2.7646
ngdeep_02703	-0.0854	2.5727	4.1288	-0.5158 ± 0.0319	0.9273	5.2440	1.8968
ngdeep_02347	1.2643	3.2795	4.0045	0.9425 ± 0.1342	0.9703	6.3713	1.9747
ngdeep_01729	2.1031	3.9039	4.5046	2.6890 ± 0.1669	2.0250	10.0765	2.9662
ngdeep_03606	1.0500	3.9821	5.0065	0.4551 ± 0.1697	1.8661	11.3734	4.2823
Average Profile	1.2498	3.3907	4.5205	1.3388 ± 0.1188	1.0304	7.1720	2.5054

Table 2. Columns 2–4 list the $\text{H}\alpha$ attenuation at 10%, 50%, and 90% of the cumulative star formation rate ($A_{10\%}^{\text{SFR}}$, $A_{50\%}^{\text{SFR}}$, $A_{90\%}^{\text{SFR}}$). Column 5 reports the global $A(\text{H}\alpha)$ derived from the integrated flux over the entire galaxy, representing the global attenuation. Columns 6–8 report the best-fit parameters for each galaxy using the error function model the amplitude (A), mean (μ), and standard deviation (σ) of the fitted profile. The above quantities for the average profile are reported in the last row.

$$\text{erf}(x) = \frac{2}{\sqrt{\pi}} \int_0^x e^{-t^2} dt \quad (9)$$

where A is amplitude, μ determines location of the turnover, and σ controls the width of the turnover. The erf is the standard error function. The best-fit parameters are presented in Table 2.

Curve fits with a low A value correspond to galaxies with less obscured star-formation overall. A fit with a low μ value indicates that most of the star formation rests in regions with low attenuation, whereas a high μ value reflects a shift toward more star formation in heavily obscured regions. Finally, fits with a small σ indicate that the star formation is concentrated around a narrow range of attenuation, while a large σ signifies that star formation is distributed across a broader range of attenuation. This parameterization allows us to summarize the curves and compare the overall shape of attenuation profiles across our galaxy sample in a simple, quantitative way. We also tested a third-degree polynomial model fit to our curves. We found that they can approximate the cumulative profiles, however they often have negative components which are unphysical in this context.

In Table 2 we present non-parametric measures of these curves, defined as $A_{10\%}^{\text{SFR}}$, $A_{50\%}^{\text{SFR}}$, and $A_{90\%}^{\text{SFR}}$.

$A_{10\%}^{\text{SFR}}$ is defined as the attenuation at $\text{H}\alpha$ associated with the 10th percentile pixel of the total integrated

SFR. This value itself provides an estimate of the attenuation level associated with the *least-dusty* regions of star formation. We measure an $A_{10\%}^{\text{SFR}}$ of ≈ 1.45 for the average profile. This relatively high value for $A_{10\%}^{\text{SFR}}$ indicates that there is very little star formation with low attenuation ($A < 1$). Similarly, $A_{50\%}^{\text{SFR}}$ corresponds to the attenuation value of the 50th percentile pixel of SFR. In other words, half of the integrated SFR will be attenuated at a greater level than $A_{50\%}^{\text{SFR}}$ and half will be attenuated at a lower level. This value can be considered a *typical* or SFR-weighted median attenuation in the galaxy. For the average profile, the value of $A_{50\%}^{\text{SFR}}$ is ≈ 3.41 mag. Half of the SFR is attenuated at greater than 3.41 mag, again highlighting the extremely dusty conditions in these galaxies. Lastly, $A_{90\%}^{\text{SFR}}$ corresponds to the attenuation of the 90th percentile of the integrated SFR. At $A_{90\%}^{\text{SFR}}$, the attenuation has a mean of ≈ 4.31 mag.

We now focus our attention on the similarities and differences in the individual profiles. We do not observe a strong dependence between a galaxy’s position in Figure 2 and whether it is above or below the average attenuation profile. Although all galaxies show a similar linear increase in attenuation from 10% to 90% cumulative SFR, there is significant galaxy to galaxy variation in both slope and amplitude of the curves. These results highlight the diversity in dust distribution and geometry across the sample.

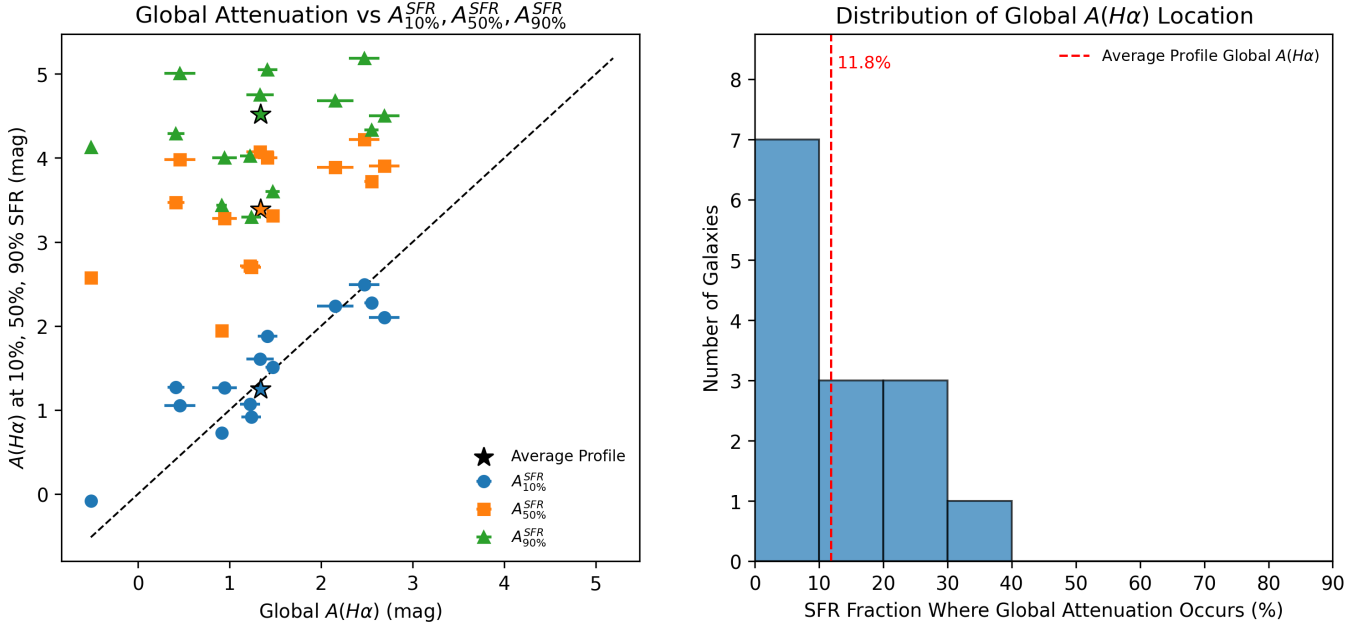


Figure 5. The left panel shows the global $A(H\alpha)$ versus the quantities $A_{10\%}^{SFR}$ (blue circle), $A_{50\%}^{SFR}$ (orange square), and $A_{90\%}^{SFR}$ (green triangle). The stars with black outlines represent the corresponding values for the average profile (see Figure 4). The right panel shows the cumulative SFR fraction corresponding to the attenuation measured globally. In short, this distribution indicates the fraction of new stars forming at or below the global attenuation level. The red dashed line indicates the SFR fraction associated with the global $A(H\alpha)$ measured for the average profile.

To help interpret these cumulative profiles, it is helpful to consider how toy dust geometries would present in Figure 4. If dust is distributed uniformly in front of the galaxy, all star-forming regions would be equally attenuated. In this case, the curves would sharply rise as a step function at a single attenuation value. This contrasts the smoother, more gradual increase observed in Figure 4. Real galaxies cannot be described by a simple uniform foreground screen. Another useful case is if dust is uniformly distributed in the galaxy. In this situation, star-forming regions that reside further in would be more obstructed than those at the surface. As a result, the cumulative profile would rise smoothly and linearly. Aside from their tails, the curves in Figure 4 all show a characteristic linear behavior. This is consistent with the expectations described above for uniform dust.

In Table 2, we also list the global $A(H\alpha)$ values for each galaxy. These are derived by summing all pixels together from the segmented $H\alpha$ and $H\beta$ maps and calculating a single (global) Balmer decrement and attenuation at $H\alpha$.

One galaxy `ngdeep_02703` exhibits nearly zero attenuation at $A_{10\%}^{SFR}$ and at global $A(H\alpha)$. The negative A values in Table 2 arise from its unphysical Balmer decrement measurements: in 72% of `ngdeep_02703`'s pixels the measured $\frac{H\alpha}{H\beta}$ falls below the intrinsic case B value of 2.86. This could be due to minor errors in the data

processing (e.g., oversubtracted backgrounds) that lead to artificially boosted $H\beta$ or reduced $H\alpha$ emission. Or it could be due to a departure from Case-B, perhaps due to gas that is optically thick to Balmer photons (C. Scarlata et al. 2024). In reality, this galaxy is probably nearly dust-free, with a Balmer decrement that is close to the intrinsic value. The negative attenuation values therefore reflect processing or measurement effects rather than actual negative extinction.

Naively, the spatially-integrated $A(H\alpha)$ should be comparable to $A_{50\%}^{SFR}$, representing the dust attenuation experienced by the median star-forming regions within a galaxy. However, comparison of the spatially-integrated $A(H\alpha)$ values in Table 2 with the cumulative profiles reveals that the integrated attenuation is instead more consistent with $A_{10\%}^{SFR}$.

In the left panel of Figure 5, we compare the spatially-integrated measurement of $A(H\alpha)$ with the attenuation value corresponding to the 10th, 50th, and 90th percentile of SFR. Here we confirm that nearly all galaxies in our sample show a close relationship between the global $A(H\alpha)$ and $A_{10\%}^{SFR}$.

In the right panel of Figure 5, we quantify the cumulative percentile associated with the global attenuation value. This panel shows the distribution of the percentile across the sample. In other words, this panel shows the fraction of the total star formation that oc-

cers at or below the globally measured $A(\text{H}\alpha)$. The histogram is strongly skewed toward low cumulative fractions, with most galaxies having their global attenuation correspond to only $\sim 5\text{--}20\%$ of the integrated SFR. For the average profile, the global $A(\text{H}\alpha)$ aligns with 11.8% of the cumulative SFR, indicated by the red dashed line. This demonstrates that the global attenuation primarily reflects the least-obsured, most luminous regions that dominate the total $\text{H}\alpha$ flux rather than the dust conditions affecting the bulk of the star formation. In other words, the integrated $A(\text{H}\alpha)$ systematically samples the low-attenuation tail of the distribution rather than the SFR-weighted median. Global measurements significantly underestimate the true level of obscuration experienced by most star formation within these galaxies.

This difference underscores the value of the cumulative attenuation analysis presented here, which provides a more nuanced view of dust obscuration across the whole galaxy. The cumulative profiles are derived on a pixel-by-pixel basis, tracing how attenuation varies across spatially distinct star-forming regions. In contrast, the global $A(\text{H}\alpha)$ compresses all regions into a single (light-weighted) average. As a result, the global attenuation often underestimates the true level of obscuration, since the global attenuation effectively only captures 10% of the total SFR leaving 90% of a galaxy's SFR unaccounted for. In this sense, relying solely on integrated measurements could lead to substantial underestimates of the total SFR and misrepresent the diversity of dust geometries within galaxies. The cumulative approach, by contrast, provides a more complete and physically meaningful characterization of internal extinction and its impact on star formation.

Overall, the cumulative profile provides a powerful and physically motivated framework for comparison with theoretical models of dust geometry and radiative transfer.

5. CONCLUSIONS

We introduce a new non-parametric technique to study the pixel-level relationship between dust attenuation and star-formation. We apply this technique on NIRISS slitless spectroscopy of 14 galaxies at $1.0 < z < 2.5$ acquired as a part of The Next Generation Deep Extragalactic Exploratory Public (NGDEEP) Survey (M. B. Bagley et al. 2023). This sample contains star-forming galaxies on or near the star formation mass sequence at their respective redshifts and spans a stellar

mass range of $10^{9.3} - 10^{10.8} M_\odot$. The primary conclusions of this paper are:

- Across the full sample, 50% of the local star formation occurs behind an attenuation of 3.41 mag or higher ($A_{50\%}^{\text{SFR}}$), indicating that the bulk of star formation in these galaxies is significantly attenuated by dust.
- A non-negligible fraction (10%) of star-formation is associated with extreme attenuation (> 4.5 mag of extinction).
- Global $A(\text{H}\alpha)$ values underestimate the *typical* obscuration of individual star-forming regions. The average global $A(\text{H}\alpha)$ corresponds to the SFR percentile of 11.8%. This indicates that the global value is biased by the brightest, least obscured regions. The global measurement fails to capture the true high attenuation impacting the light of the bulk of newly forming stars.

Our results demonstrate the power of JWST slitless spectroscopy, combined with our new non-parametric measure of local star formation and attenuation, to probe internal dust and star formation structures in galaxies at the peak of cosmic activity. The measurement introduced here allows us to directly quantify how much star formation is distributed across different levels of obscuration, providing a physically intuitive, probabilistic description of the dusty conditions experienced by star-forming regions within individual galaxies. In doing so, it offers a fundamentally new view compared to traditionally used global (light-weighted) measurements. Our results reveal obscuration that would otherwise be underestimated by these traditional measurements. As JWST continues to expand the frontier of high resolution infrared spectroscopy, future studies incorporating larger, more diverse samples especially those probing lower mass systems and extending to even higher redshifts will refine our understanding of the processes governing galaxy growth and star formation during this pivotal epoch in cosmic history.

ACKNOWLEDGMENTS

The author acknowledges support from the NASA Connecticut Space Grant Consortium. We thank the NGDEEP collaboration for their dedication and for providing the datasets used in this work. This research made use of observations and data obtained through the NGDEEP program from JWST.

Facilities: JWST

REFERENCES

Aghanim, N., Akrami, Y., Ashdown, M., et al. 2020, Planck2018 results: VI. Cosmological parameters, *Astronomy & Astrophysics*, 641, A6, doi: [10.1051/0004-6361/201833910](https://doi.org/10.1051/0004-6361/201833910)

Bagley, M. B., Pirzkal, N., Finkelstein, S. L., et al. 2023, The Next Generation Deep Extragalactic Exploratory Public (NGDEEP) Survey, <https://arxiv.org/abs/2302.05466>

Baker, J. G., & Menzel, D. H. 1938, Physical Processes in Gaseous Nebulae. III. The Balmer Decrement., *ApJ*, 88, 52, doi: [10.1086/143959](https://doi.org/10.1086/143959)

Beckwith, S. V. W., Stiavelli, M., Koekemoer, A. M., et al. 2006, The Hubble Ultra Deep Field, *AJ*, 132, 1729, doi: [10.1086/507302](https://doi.org/10.1086/507302)

Boquien, M., Burgarella, D., Roehlly, Y., et al. 2019, CIGALE: a python Code Investigating GALaxy Emission, *Astronomy & Astrophysics*, 622, A103, doi: [10.1051/0004-6361/201834156](https://doi.org/10.1051/0004-6361/201834156)

Brammer, G. 2022, grizli, 1.5.0 Zenodo, doi: [10.5281/zenodo.7351572](https://doi.org/10.5281/zenodo.7351572)

Calzetti, D. 1997, in AIP Conference Proceedings (AIP), doi: [10.1063/1.53764](https://doi.org/10.1063/1.53764)

Dale, D. A., Helou, G., Magdis, G. E., et al. 2014, A TWO-PARAMETER MODEL FOR THE INFRARED/SUBMILLIMETER/RADIO SPECTRAL ENERGY DISTRIBUTIONS OF GALAXIES AND ACTIVE GALACTIC NUCLEI, *The Astrophysical Journal*, 784, 83, doi: [10.1088/0004-637X/784/1/83](https://doi.org/10.1088/0004-637X/784/1/83)

Estrada-Carpenter, V., Papovich, C., Momcheva, I., et al. 2019, CLEAR. I. Ages and Metallicities of Quiescent Galaxies at $1.0 \leq z \leq 1.8$ Derived from Deep Hubble Space Telescope Grism Data, *ApJ*, 870, 133, doi: [10.3847/1538-4357/aaf22e](https://doi.org/10.3847/1538-4357/aaf22e)

Fukugita, M., Ichikawa, T., Gunn, J. E., et al. 1996, The Sloan Digital Sky Survey Photometric System, *AJ*, 111, 1748, doi: [10.1086/117915](https://doi.org/10.1086/117915)

Förster Schreiber, N. M., & Wuyts, S. 2020, Star-Forming Galaxies at Cosmic Noon, *Annual Review of Astronomy and Astrophysics*, 58, 661–725, doi: [10.1146/annurev-astro-032620-021910](https://doi.org/10.1146/annurev-astro-032620-021910)

Gardner, J. P., Mather, J. C., Abbott, R., et al. 2023, The James Webb Space Telescope Mission, *PASP*, 135, 068001, doi: [10.1088/1538-3873/acd1b5](https://doi.org/10.1088/1538-3873/acd1b5)

Hemmati, S., Mobasher, B., Darvish, B., et al. 2015, NEBULAR AND STELLAR DUST EXTINCTION ACROSS THE DISK OF EMISSION-LINE GALAXIES ON KILOPARSEC SCALES, *The Astrophysical Journal*, 814, 46, doi: [10.1088/0004-637X/814/1/46](https://doi.org/10.1088/0004-637X/814/1/46)

Kennicutt, R. C., & Evans, N. J. 2012, Star Formation in the Milky Way and Nearby Galaxies, *ARA&A*, 50, 531, doi: [10.1146/annurev-astro-081811-125610](https://doi.org/10.1146/annurev-astro-081811-125610)

Madau, P., & Dickinson, M. 2014, Cosmic Star-Formation History, *Annual Review of Astronomy and Astrophysics*, 52, 415–486, doi: [10.1146/annurev-astro-081811-125615](https://doi.org/10.1146/annurev-astro-081811-125615)

Matharu, J., Muzzin, A., Brammer, G. B., et al. 2021, HST/WFC3 Grism Observations of $z \sim 1$ Clusters: Evidence for Rapid Outside-in Environmental Quenching from Spatially Resolved H α Maps, *The Astrophysical Journal*, 923, 222, doi: [10.3847/1538-4357/ac26c3](https://doi.org/10.3847/1538-4357/ac26c3)

Matharu, J., Muzzin, A., Sarrouh, G. T. E., et al. 2023, A First Look at Spatially Resolved Balmer Decments at $1.0 \leq z \leq 2.4$ from JWST NIRISS Slitless Spectroscopy, *ApJL*, 949, L11, doi: [10.3847/2041-8213/acd1db](https://doi.org/10.3847/2041-8213/acd1db)

Matharu, J., Muzzin, A., Sarrouh, G. T. E., et al. 2023, A First Look at Spatially Resolved Balmer Decments at $1.0 < z < 2.4$ from JWST NIRISS Slitless Spectroscopy, *The Astrophysical Journal Letters*, 949, L11, doi: [10.3847/2041-8213/acd1db](https://doi.org/10.3847/2041-8213/acd1db)

Matharu, J., Nelson, E. J., Brammer, G., et al. 2024, A first look at spatially resolved star formation at $4.8 \leq z \leq 6.5$ with JWST FRESCO NIRCam slitless spectroscopy, *A&A*, 690, A64, doi: [10.1051/0004-6361/202450522](https://doi.org/10.1051/0004-6361/202450522)

Matharu, J., Shen, L., Shavaei, I., et al. 2025, A first look at a complete view of spatially resolved star formation at $1 \leq z \leq 1.8$ with JWST NGDEEP+FRESCO slitless spectroscopy, *arXiv e-prints*, arXiv:2511.15792, <https://arxiv.org/abs/2511.15792>

McCliment, W., Tacchella, S., D'Eugenio, F., et al. 2024, The density-bounded twilight of starbursts in the early Universe, <https://arxiv.org/abs/2405.15859>

Menzel, D. H., & Baker, J. G. 1937, Physical Processes in Gaseous Nebulae. II. Theory of the Balmer Decrement, *ApJ*, 86, 70, doi: [10.1086/143844](https://doi.org/10.1086/143844)

Momcheva, I. G., Lee, J. C., Ly, C., et al. 2013, Nebular Attenuation in H α -selected Star-forming Galaxies at $z = 0.8$ from the NewH α Survey, *AJ*, 145, 47, doi: [10.1088/0004-6256/145/2/47](https://doi.org/10.1088/0004-6256/145/2/47)

Nelson, E. J., van Dokkum, P. G., Momcheva, I. G., et al. 2016, Spatially Resolved Dust Maps from Balmer Decments in Galaxies at $z \sim 1.4$, *ApJL*, 817, L9, doi: [10.3847/2041-8205/817/1/L9](https://doi.org/10.3847/2041-8205/817/1/L9)

Noirot, G., Desprez, G., Asada, Y., et al. 2023, The first large catalogue of spectroscopic redshifts in Webb's first deep field, SMACS J0723.3-7327, *Monthly Notices of the Royal Astronomical Society*, 525, 1867–1884, doi: [10.1093/mnras/stad1019](https://doi.org/10.1093/mnras/stad1019)

Oke, J. B., & Gunn, J. E. 1983, Secondary standard stars for absolute spectrophotometry., *ApJ*, 266, 713, doi: [10.1086/160817](https://doi.org/10.1086/160817)

Osterbrock, D. E., & Ferland, G. J. 2006, Astrophysics of gaseous nebulae and active galactic nuclei

Papovich, C., Simons, R. C., Estrada-Carpenter, V., et al. 2022, CLEAR: The Ionization and Chemical-enrichment Properties of Galaxies at $1.1 < z < 2.3$, *The Astrophysical Journal*, 937, 22, doi: [10.3847/1538-4357/ac8058](https://doi.org/10.3847/1538-4357/ac8058)

Park, H.-J., Battisti, A. J., Wisnioski, E., et al. 2024, The spatially resolved relation between dust, gas, and metal abundance with the TYPHOON survey, <https://arxiv.org/abs/2410.02222>

Pirzkal, N., Rothberg, B., Ryan, R. E., et al. 2018, A Two-dimensional Spectroscopic Study of Emission-line Galaxies in the Faint Infrared Grism Survey (FIGS). I. Detection Method and Catalog, *ApJ*, 868, 61, doi: [10.3847/1538-4357/aae585](https://doi.org/10.3847/1538-4357/aae585)

Pirzkal, N., Rothberg, B., Papovich, C., et al. 2024, The Next Generation Deep Extragalactic Exploratory Public Near-infrared Slitless Survey Epoch 1 (NGDEEP-NISSL): Extragalactic Star-formation and Active Galactic Nuclei at $0.5 < z < 3.6$, *ApJ*, 969, 90, doi: [10.3847/1538-4357/ad429c](https://doi.org/10.3847/1538-4357/ad429c)

Reddy, N. A., Shapley, A. E., Kriek, M., et al. 2020, The MOSDEF Survey: The First Direct Measurements of the Nebular Dust Attenuation Curve at High Redshift, *ApJ*, 902, 123, doi: [10.3847/1538-4357/abb674](https://doi.org/10.3847/1538-4357/abb674)

Salim, S., & Narayanan, D. 2020, The Dust Attenuation Law in Galaxies, *Annual Review of Astronomy and Astrophysics*, 58, 529–575, doi: [10.1146/annurev-astro-032620-021933](https://doi.org/10.1146/annurev-astro-032620-021933)

Scarlata, C., Hayes, M., Panagia, N., et al. 2024, On the universal validity of Case B recombination theory, <https://arxiv.org/abs/2404.09015>

Shen, L., Papovich, C., Matharu, J., et al. 2024, NGDEEP Epoch 1: Spatially Resolved H α Observations of Disk and Bulge Growth in Star-Forming Galaxies at $z \sim 0.6$ –2.2 from JWST NIRISS Slitless Spectroscopy, <https://arxiv.org/abs/2310.13745>

Shen, L., Papovich, C., Matharu, J., et al. 2025, NGDEEP: The Star Formation and Ionization Properties of Galaxies at $1.7 < z < 3.4$, *ApJL*, 980, L45, doi: [10.3847/2041-8213/adb28d](https://doi.org/10.3847/2041-8213/adb28d)

Simons, R. C., Papovich, C., Momcheva, I., et al. 2021, CLEAR: The Gas-phase Metallicity Gradients of Star-forming Galaxies at $0.6 < z < 2.6$, *The Astrophysical Journal*, 923, 203, doi: [10.3847/1538-4357/ac28f4](https://doi.org/10.3847/1538-4357/ac28f4)

Simons, R. C., Papovich, C., Momcheva, I. G., et al. 2023, CLEAR: Survey Overview, Data Analysis, and Products, *The Astrophysical Journal Supplement Series*, 266, 13, doi: [10.3847/1538-4365/acc517](https://doi.org/10.3847/1538-4365/acc517)

Tacchella, S., Carollo, C. M., Förster Schreiber, N. M., et al. 2018, Dust Attenuation, Bulge Formation, and Inside-out Quenching of Star Formation in Star-forming Main Sequence Galaxies at $z \sim 2$, *ApJ*, 859, 56, doi: [10.3847/1538-4357/aabf8b](https://doi.org/10.3847/1538-4357/aabf8b)

Wang, W., Faber, S. M., Liu, F. S., et al. 2017, UVI colour gradients of $0.4 < z < 1.4$ star-forming main-sequence galaxies in CANDELS: dust extinction and star formation profiles, *Monthly Notices of the Royal Astronomical Society*, 469, 4063, doi: [10.1093/mnras/stx1148](https://doi.org/10.1093/mnras/stx1148)

Wang, X., Jones, T., Vulcani, B., et al. 2022, Early Results from GLASS-JWST. IV. Spatially Resolved Metallicity in a Low-mass $z \sim 3$ Galaxy with NIRISS, *ApJL*, 938, L16, doi: [10.3847/2041-8213/ac959e](https://doi.org/10.3847/2041-8213/ac959e)

Watson, P. J., Vulcani, B., Treu, T., et al. 2025, The GLASS-JWST Early Release Science programme: The NIRISS spectroscopic catalogue, *Astronomy & Astrophysics*, 699, A225, doi: [10.1051/0004-6361/202554954](https://doi.org/10.1051/0004-6361/202554954)

Whitaker, K. E., Franx, M., Leja, J., et al. 2014, CONSTRAINING THE LOW-MASS SLOPE OF THE STAR FORMATION SEQUENCE AT $0.5 < z < 2.5$, *The Astrophysical Journal*, 795, 104, doi: [10.1088/0004-637x/795/2/104](https://doi.org/10.1088/0004-637x/795/2/104)

Wuyts, S., Förster Schreiber, N. M., Genzel, R., et al. 2012, SMOOTH(ER) STELLAR MASS MAPS IN CANDELS: CONSTRAINTS ON THE LONGEVITY OF CLUMPS IN HIGH-REDSHIFT STAR-FORMING GALAXIES, *The Astrophysical Journal*, 753, 114, doi: [10.1088/0004-637X/753/2/114](https://doi.org/10.1088/0004-637X/753/2/114)

Yang, G., Boquien, M., Buat, V., et al. 2019, x-cigale: fitting AGN/galaxy SEDs from X-ray to infrared, *Monthly Notices of the Royal Astronomical Society*, 491, 740, doi: [10.1093/mnras/stz3001](https://doi.org/10.1093/mnras/stz3001)